RSC Advances

PAPER

View Article Online
View Journal | View Issue

Cite this: *RSC Adv.*, 2024, **14**, 36461

Hydroxyapatite supported molybdenum oxide catalyst for selective dehydrogenation of cyclohexane to cyclohexene: studies of dispersibility and chemical environment

Mingxiao Zheng,[a] Feng Zhou,[b] Huixia Ma,[b] Xuefeng Song[a] and Guang Wu *[a]

The selective oxidative dehydrogenation of cyclohexane to cyclohexene was conducted using molybdenum oxide (MoO_x) as a catalyst and hydroxyapatite (HAP) and $Ca_5(OH)(PO_4)_3$ as carriers. Two series of MO_x/HAP catalysts with varying MoO_x loading capacity and calcination temperature were prepared *via* the co-impregnation method. The impact of dispersibility and chemical environment on the catalytic performance of MoO_x was investigated. The catalysts were characterized using XRD, XPS, H_2-TPR, and UV-Vis spectra. These MoO_x/HAP catalysts were employed for the oxidative dehydrogenation (ODH) of cyclohexane to cyclohexene. MoO_x/HAP catalysts with lower loading capacity exhibited higher dispersion of MoO_x and selectivity towards cyclohexane. The calcination temperature directly influenced the chemical environment of MoO_x, thereby affecting its catalytic performance. Samples calcinated at lower temperatures (500 °C and 600 °C) demonstrated higher conversion rates for cyclohexane, while samples calcinated at higher temperatures (above 700 °C) displayed greater selectivity towards cyclohexane. At 430 °C, when the conversion rate of cyclohexane reached 13.1%, the selectivity of cyclohexene over MHAP-0.05-800 catalyst reached 58.2%.

Received 30th August 2024
Accepted 25th October 2024

DOI: 10.1039/d4ra06259k

rsc.li/rsc-advances

Introduction

Cyclohexene is an ideal raw material for the synthesis of cyclohexanol, cyclohexanone, and adipic acid, which are in high demand in the chemical fiber industry. Due to its active double bond and six-membered ring structure, cyclohexene is also widely used in the production of fine chemicals such as pharmaceuticals, pesticides, dyes, detergents, feed additives, and polyester.[1,2] Currently, the main methods for producing cyclohexene include catalytic dehydration of cyclohexanol, dehalogenation of halogenated cyclohexane, and selective hydrogenation of benzene.[3,4] The raw material costs associated with the first two routes are relatively high and involve highly corrosive inorganic acids during the production processes. This increases equipment costs as well as environmental expenses. The selective hydrogenation of benzene to synthesize cyclohexene offers both availability and cost-effectiveness while aligning with the principles of atomic economy and environmental sustainability. However, its selectivity for producing pure cyclohexene is relatively low resulting in approximately 30% by-product formation of cyclohexane. Oxidative dehydrogenation (ODH) of cyclohexane to produce cyclohexene has gained significant attention due to its potential practical applications.[5–7] In theory, cyclohexane exhibits thermodynamic stability compared to benzene; however, cyclohexane demonstrates higher reactivity making it prone to hydrogenate into cyclohexane or further dehydrogenate into benzene. The direct dehydrogenation process requires high reaction temperatures which can lead to carbon chain fragmentation or extensive coking. On top that, the process suffers from poor product selectivity along with short catalyst lifespan.[8,9] Conversely, the ODH method reduces both reaction temperature requirements and carbon deposition on catalyst surfaces thereby extending catalyst lifespan. Hence, it has become a viable research approach for synthesizing cyclohexane. Therefore, it has become a feasible research approach for cyclohexene synthesis.

The catalyst system serves as the fundamental component of the ODH process. Various catalytic systems have been reported for cyclohexene production through ODH, with particular attention given to vanadium-containing systems, molybdenum oxide systems, and other metal oxide catalysts.[10–12] However, undesired CO_x and benzene byproducts often result from deep oxidation and dehydrogenation.[13–15] While V^{5+} exhibits excellent C–H bond activation in hydrocarbon molecules, the presence of V=O in its structure promotes the formation of C–O bonds and its high affinity for C–C bond dissociation, leading to a significant amount of CO_x in the final product.[16–19] MoO_3 possesses an

[a]*School of Chemistry and Materials Sciences, Research Institute of Crop Science, Heilongjiang University, Harbin 150080, China. E-mail: Wu.guang@163.com*
[b]*Dalian Reserch Institute of Petroleum and Petrochemicals, SINOPEC, Dalian 116045, China*

acidic non-stoichiometric octahedral oxide structure with numerous oxygen vacancies. The REDOX reactions between Mo^{5+} and Mo^{6+} maintain a dynamic balance between structural defects and gas-phase oxygen. The octahedral structure of Mo^{6+} facilitates deep oxidation reactions, while the saturation coordination structure of Mo^{5+} enhances olefin selectivity in ODH reactions.[20] Therefore, molybdenum-based catalysts not only offer potential for highly selective olefin production during ODH reactions but also their composition significantly influences cycloalkane ODH reactions.

It has been reported that a supported MoO_x catalyst is an important catalytic system for alkane ODH.[21–23] Effective reactant activation directly depends on the local structure of the catalyst, distribution of metal oxides on the carrier surface, and parameters related to catalyst preparation processes.[24–26] The supported MoO_x catalyst undergoes a transition from isolated monomers to larger polymolybdates due to submonolayer coverage on supports. Depending on different surface densities of Mo and sample preparation conditions, large crystals of MoO_x form on carriers when single-layer coverage is exceeded.[27,28] Hydroxyapatite (HAP), as a carrier with both acid–base properties, high stability and easy substitution of heterogeneous elements, has been deeply studied in acid–base dependent catalytic reactions.[29,30] In addition, it was found that the phosphate in HAP can change the electronic environment of heterogeneous metals, promote their high dispersion, and promote the stability of the catalyst through strong metal–support interactions.[31,32] Based on the above characteristics, HAPs as catalyst support has shown excellent performance in catalytic reactions.[33,34]

The dispersity of MoO_x on various surfaces is dependent on the specific carrier, the surface density of Mo, and the calcination temperature of the sample. This dispersity has a significant impact on catalytic reaction performance. Although there have been reports on MoO_x in REDOX reactions, there are limited studies on the synthesis of HAP-supported MoO_x catalysts and their catalytic ODH reactions. Furthermore, the influence of MoO_x content and chemical environment on ODH catalytic performance remains largely unexplored. In this study, a molybdenum oxide catalyst supported by HAP was synthesized using coprecipitation method under different MoO_x content and calcination temperatures. The effects of synthesis method on catalyst structure and its impact on ODH catalytic performance were investigated. Additionally, the role of different MoO_x species in cyclohexane ODH reaction was revealed.

Materials and methods

Materials

Ammonium molybdate ($(NH_4)_6Mo_7O_{24}\cdot 4H_2O$, ≥99%), HAP ($Ca_{10}(PO_4)_6(OH)_2$, ≥99%), were obtained from Alpha Chemical Reagent Co., Ltd (Tianjin, China).

Preparation of catalysts

The support material was impregnated using an incipient wetness method. Corresponding amounts of $(NH_4)_6Mo_7O_{24}\cdot 4H_2O$ to the aimed nominal MoO_3 loadings were dissolved in 5 mL demineralized water. The impregnation solution was thoroughly mixed with commercial HAP (Ca/P = 1.67) using glass rods for 5 minutes and dried overnight at 80 °C. The impregnated sample was then calcined in a Muffle furnace under still air at 550 °C for 4 hours at a heating rate of 5 °C min^{-1}.

Two series of catalysts were prepared based on different loading amounts and calcination temperatures: MHAP-*x*-*y* (where *x* represents the Mo/Ca ratio, $x = 0.025$, 0.05, 0.075, and 0.1; *y* represents the calcination temperature, y = 500 °C, 600 °C, 700 °C, 800 °C).

Characterization

The chemical composition of the sample was determined using an SRS-3400 X-ray fluorescence analyzer (XRF). The nitrogen adsorption–desorption isotherm of the sample was measured using a Quantachrome AUTOSORB-1-MP physical adsorption instrument to obtain information about its surface and structure characteristics. The surface area (S_{BET}) of the sample was calculated using the BET method. Powder X-ray diffraction (XRD) patterns were recorded for synthesized MoO_x/HAP samples using CuKα radiation intensity at ARL X'TRA powder diffractometer. X-ray photoelectron spectroscopy (XPS) measurements were conducted using PHI1600 XPS system radiated by AlKα radiation to determine binding energies for elements such as Mo (3d) and O (1s). A diffuse reflectance UV-Vis spectrum was obtained on a HITECHI U-3900 UV-Vis-NIR spectrometer, with $BaSO_4$ as a reference material. The samples were ground, then placed in a diffuse sample tank, pressed with a cover glass and placed in the sample card tank, and recorded at room temperature in the test range of 200–1000 nm. The reflectivity of the standard carrier was used as the basis for the determination of the sample. Temperature programmed reduction (H_2-TPR) experiments were conducted on a chemisorption analyzer provided by Dalian University of Technology. The samples were pretreated at 300 °C in an Ar (40 mL min^{-1}) for 2 hours, followed by cooling to 25 °C. Subsequently, the sample underwent reduction from 25 °C to 850 °C at a heating rate of 10 °C min^{-1} under a flow rate of 10% H_2/Ar (40 mL min^{-1}). The amount of H_2 consumed by the sample was measured using a TCD detector to obtain the H_2-TPR curve. Transmission electron microscopy (TEM) analysis was performed using a JEOL-JEM-2100F electron microscope operating at 200 kV. The acidity properties of the sample were studied through NH_3-temperature-programmed desorption (NH_3-TPD) technique. Prior to testing, the catalyst underwent pretreatment in Ar stream at 500 °C for 2 hours and then cooled down to 100 °C for NH_3 adsorption before being purged with argon again. During TPD experiment, temperature increased from 100 °C to 850 °C at a heating rate of 10 °C min^{-1} while monitoring desorbed NH_3 with TCD detector.

Catalyst performance

The catalytic reaction took place in a miniature fixed bed reactor with an inner diameter of 8 mm. The catalyst weighing 0.5 g was

compressed into uniform particles ranging between 20–40 mesh before being placed inside the reaction tube's constant temperature zone. Prior to running any reactions, the system underwent air purification at a rate of 40 mL min^{-1} for one hour at 500 °C for 1 h. After being cooled to the reaction temperature, cyclohexane was introduced *via* pumping, and samples were analyzed at intervals of 1 hour. The reaction operated with a space speed of 6 h^{-1} and a molar ratio of cyclohexane to O_2 of 2 : 1. The experiments were conducted under atmospheric pressure within the temperature range of 400–490 °C.

For quantitative analysis of product composition, an on-line gas chromatography (GC) system Agilent 6890 equipped with a flame detector (FID) and an HP-5 column (Agilent, dimensions: 60 m × 0.32 mm i.d × 0.5 μm) was employed. Cyclohexane conversion, product selectivity, and TOF values are calculated using eqn (1)–(3) respectively.

$$\text{Con}\ (\%) = \frac{n_{C_6H_{12}(\text{inlet})} - n_{C_6H_{12}(\text{outlet})}}{n_{C_6H_{12}(\text{inlet})}} \times 100 \quad (1)$$

$$\text{Sel}\ (\%) = \frac{n_i \times n_{i(\text{outlet})}}{\sum n_i \times n_{i(\text{outlet})}} \times 100\% \quad (2)$$

$$\text{TOF}_{C_6H_{10}} = \frac{\left(n_{C_6H_{12},\text{in}} - n_{C_6H_{12},\text{out}}\right) \times \text{NA}}{\text{total number of Mo atoms}} \times \text{Sel}_{C_6H_{10}} \quad (3)$$

Results and discussion

Physical and textural properties

XRF spectroscopy was employed to analyze the elemental composition of all samples, and the results are presented in Table 1. All samples exhibited similar Ca/P ratios, ranging from 1.7 to 1.8. The Mo/Ca ratio of MO_x/HAP samples increased with increasing Mo addition, while the Mo/Ca ratio remained relatively consistent across different roasting temperatures.

Table 1 provides BET surface area values for all samples. With an increase in Mo content, the surface area of MO_x/HAP samples gradually decreased with varying amounts of MoO_x, which is consistent with the behavior observed in most supported catalyst materials regarding specific surface area variation. The BET surface area of MO_x/HAP samples with different calcination temperatures decreased from 48.6 m^2 g^{-1} (MHAP-0.05-500) to 8.4 m^2 g^{-1} (MHAP-0.05-800) as the calcination temperature increased, indicating particle agglomeration due to calcination.

Table 1 Elemental compositions, BET surface area and UV-Vis edge energies (E_g) of the MO_x/HAP samples

Samples	Ca/P ratios	Mo/Ca ratios	Surface area (m^2 g^{-1})	E_g (eV)
MHAP-0.025-550	4.3	0.03	49.5	3.23
MHAP-0.05-550	4.3	0.06	41.6	3.25
MHAP-0.075-550	4.3	0.09	37.3	3.11
MHAP-0.1-550	4.3	0.11	30.6	3.03
MHAP-0.05-500	4.3	0.06	48.6	3.20
MHAP-0.05-600	4.3	0.06	26.5	3.41
MHAP-0.05-700	4.3	0.06	10.7	3.70
MHAP-0.05-800	4.3	0.06	8.4	3.43

Fig. 1(a) and (b) depict XRD patterns of MO_x/HAP catalysts with different MoO_x amounts and calcination temperatures respectively, alongside references showing XRD patterns of $CaMoO_4$ and HAPs samples in Fig. 1. No presence of a MoO_3 phase was detected in any sample, suggesting that MoO_x was effectively dispersed on the carrier's surface. However, a diffraction peak corresponding to $CaMoO_4$ appeared in the sample due to partial substitution by Mo atoms occupying P positions in HAP structure. The strength of this peak increased with higher levels of added MoO_x content signifying greater incorporation into HAP's crystal structure. As shown in Fig. 1(b), $CaMoO_4$ began appearing at a low calcination temperature of 500 °C and its crystal diffraction peak intensified as calcination temperature rose. This indicates that elevated calcination temperatures facilitated more significant infiltration of Mo into the HAP lattice, resulting in P–O–Mo or Ca–O–Mo structures. Fig. 1(b) demonstrates that when calcination temperature reached 700 °C, $Ca_3(PO_4)_2$ crystals emerged, suggesting that high-temperature calcination removes part of the hydroxyl group in HAP.

The valence state of Mo in the catalyst was further determined by XPS analysis. The XPS spectra of Mo 3d (Fig. 2) reveal that the double peaks at 233.1 eV and 236.3 eV can be attributed to Mo $3d_{5/2}$ and Mo $3d_{2/3}$, respectively, indicating the presence of Mo^{6+} species (Fig. 2(a) and (b)).[35–37] According to previous studies, there is an additional peak at 233.7 eV, which corresponds to the Mo^{5+} species.[38] By classifying and integrating

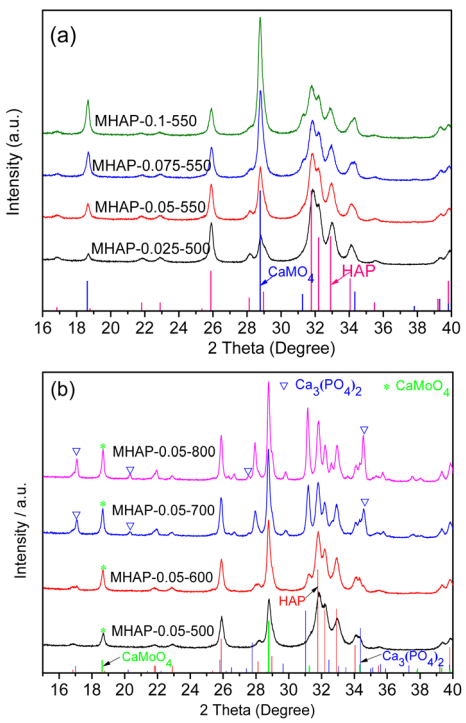

Fig. 1 XRD patterns of HAPs, $CaMoO_4$, $Ca_3(PO_4)_2$ and MO_x/HAP with different MoO_x loading amounts (a) and calcination temperature (b).

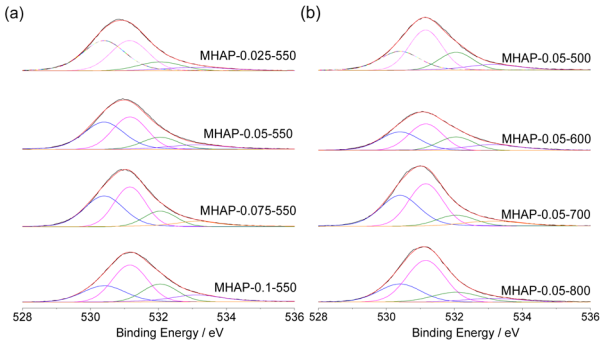

Fig. 2 Mo 3d XPS spectra of MO_x/HAP with different MoO_x loading amounts (a) and calcination temperature (b).

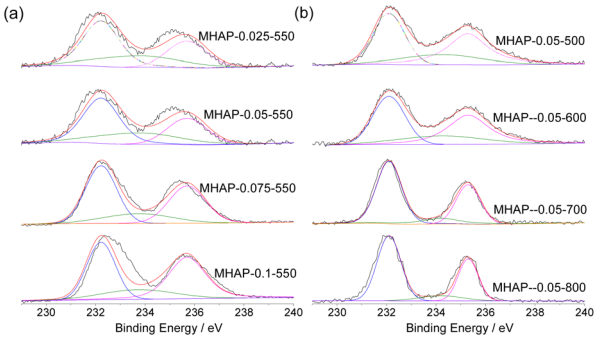

Fig. 3 O 1s XPS spectra of MO_x/HAP with different Mo loading amounts (a) and calcination temperature (b).

these peaks, changes in the distribution of different oxidation states of Mo were discussed. The results are summarized in Table 2. Although the diffraction peak corresponding to crystalline MoO_3 is not observed in the XRD pattern due to its small particle size, it can be concluded that under low calcination temperature, most of the Mo on HAP surface are still associated with dispersed MoO_x compounds. Table 2 demonstrates that as the loading amount of MoO_x increases, there is a successive decrease in the proportion of Mo^{5+} species accompanied by an increase in the content of Mo^{6+}. This suggests a direct relationship between dispersity and Mo valence distribution; highly dispersed samples contain more amounts of Mo^{5+}. Furthermore, increasing calcination temperature significantly reduces the proportion of Mo^{5+}, with a sharp decline observed at 700 °C. The XRD results indicate that as calcination temperature rises, the incorporation of Mo into HAP lattice increases, resulting in a decrease in the amount of Mo^{5+}. The most significant reduction occurs at 700 °C.

The deconvolution XPS spectra of O 1s shown in Fig. 3(a) and (b) exhibit four distinct peaks located at binding energies 530.5 eV, 531.2 eV, 532.1 eV, and 533.1 eV, respectively. These peaks are attributed to Mo–O,[39] lattice oxygen, oxygen vacancy, and O–H.[40–42] Table 2 summarizes the area ratios for each binding energy range obtained from different catalysts. The XPS spectrum of O reveals that the Mo–O bond increases with an increase in MO_x loading amount. This demonstrates an increase in the number of MO_x crystals on the carrier surface. Lattice oxygen primarily originates from the P–O bond within the PO_4^{3-}. As MO_x amount increases, both lattice oxygen and O vacancy decrease, indicating a greater substitution of Mo at the P position and penetration into O vacancy. For samples subjected to different calcination temperatures, a gradual reduction in OH concentration (533.1 eV) are observed as calcination temperature rises, suggesting dehydroxylation of HAP during this process. Dehydroxylation leads to the creation of new defect sites upon removal of hydroxyl groups. At calcination temperatures between 500–600 °C, only a slight increase in O vacancy is observed. However, when reaching 700 °C, there is a significant decrease in OH content without a corresponding increase in O vacancy due to MoO_x filling these vacancies instead. In other words, formation of O vacancy promotes MoO_x infiltration into these regions resulting in better dispersion and simultaneous formation of P–O–Mo or Ca–O–Mo structures.

The effect of weight loading and calcination temperature on the formation of catalytic sites was further investigated by UV-Vis diffuse reflectance spectroscopy to determine bandgaps for MO_x/HAP samples (Fig. 4). As shown by Chakrabarti and Wachs, lower bandgap values of Mo supported on Al_2O_3 indicate larger molybdenum clusters (>1 nm) on the surface, and higher bandgaps translate to smaller dimeric and monomeric (<1 nm) MoO_x species on the support.[43] A broad feature at 320 nm is assigned to polymeric MoO_x while 245 nm is attributed to oligomeric MoO_x species. At lower loadings (MHAP-0.025-550), the isolated, oligomeric species dominated while at higher loadings (MHAP-0.05-550, MHAP-0.075-550 and MHAP-0.1-550) there was more polymeric species in addition to oligomeric MoO_x. As weight loading was increased, the bandgap fell, due to larger oxide clusters forming, as also shown in

Table 2 The deconvolution results of the O 1s XPS spectra of MHAP

		Proportion of area (%)							
Band	BE (eV)	Mo-0.025-550	Mo-0.05-550	Mo-0.075-550	Mo-0.1-550	Mo-0.05-500	Mo-0.05-600	Mo-0.05-700	Mo-0.05-800
Mo^{5+}	233.7	25.2	24.1	17.4	17.0	18.7	18.3	11.0	8.4
Mo^{6+}	235.2 and 231.1	74.8	75.9	82.6	83.0	81.3	81.7	89.0	91.6
Mo–O	530.4	24.1	39.4	38.5	44.4	27.2	30.2	38.6	40.1
Lattice oxygen	531.1	41.8	36.4	36.8	35.7	41.9	36.7	41.3	41.7
Oxygen vacancy	532.0	20.0	14.6	14.8	12.1	17.3	16.4	11.9	11.2
O–H	533.1	14.1	9.6	9.8	7.8	13.6	16.6	8.2	7.1

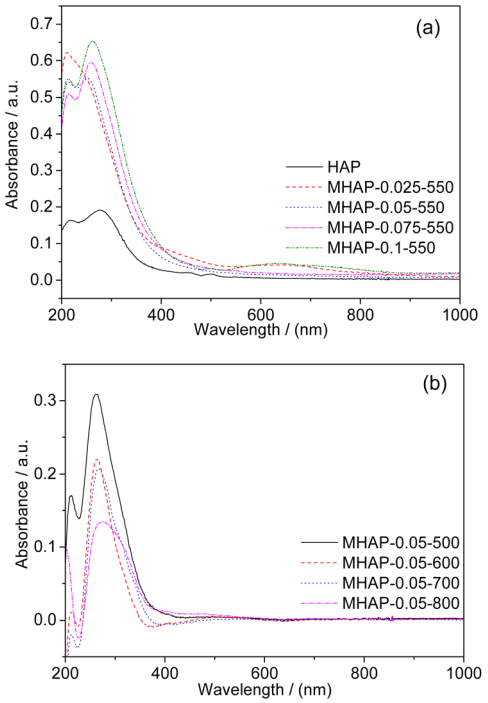

Fig. 4 Diffuse reflectance UV-Vis spectra for HAPs and MO_x/HAP samples with different Mo loading amounts (a) and calcination temperature (b).

Fig. 4(a). The band of MoO_x with the high-temperature calcinated sample, as shown in Fig. 5(b), exhibits enhanced sharpness, thereby contributing to the increased crystallinity of MoO_x on the HAP surface. However, the band intensity of high

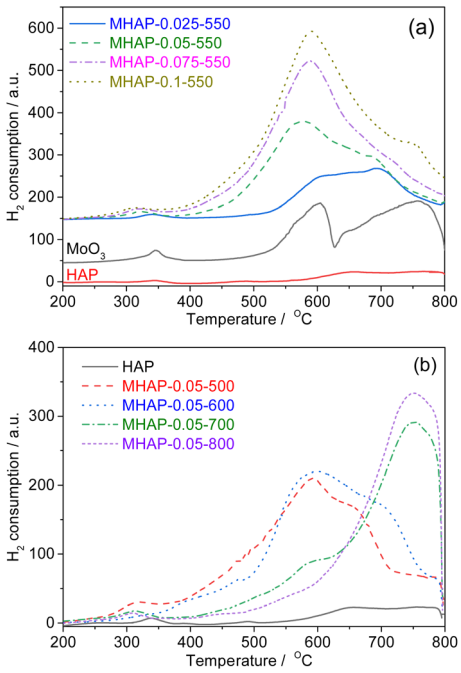

Fig. 5 H_2-TPR patterns of HAP, MoO_3 and MO_x/HAP samples with different Mo loading amounts (a) and calcination temperature (b).

temperature calcinated samples decreased significantly, which was due to the increase of Mo entering HAP lattice under high temperature calcination.

Fig. 5(a) illustrates the H_2-TPR profiles of MoO_3, HAP, and supported molybdenum oxide samples. Notably, there is minimal reduction peak observed in HAP. Generally, the reduction pathway of molybdenum species can be described as follows:[44]

$$MoO_3 + H_2 \rightarrow MoO_2 + H_2O$$

$$MoO_2 + H_2 \rightarrow Mo^0 + 2H_2O$$

The first reaction involves the reduction of MoO_3 to MoO_2 within a temperature range of 500–630 °C. On the other hand, the second reaction occurs at temperatures between 630–800 °C and leads to the reduction of MoO_2 to Mo^0.[45] In contrast, HAP-loaded MoO_x exhibits a distinct low temperature reduction peak and lacks an obvious high temperature reduction peak, indicating a strong interaction between MoO_x and the carrier. As the load increases, it is reasonable for the peak area to gradually increase. The disparity between samples prepared at different calcination temperatures becomes more pronounced due to the significant influence of oxide structure on the reducibility of molybdenum oxides.[46] A distinct low-temperature reduction peak is observed in samples calcined below 600 °C, while this peak disappears when the calcination temperature exceeds 700 °C, indicating an almost complete disappearance of independent MoO_3. Reduction peaks around 750 °C are attributed to strongly interacting MoO_x species with the carrier and partially incorporated Mo species within the HAP lattice. This suggests that the oxidation state of Mo in the catalyst is significantly influenced by high-temperature treatment.

The HRTEM images of the MHAP catalyst after calcination at 600 °C and 800 °C are presented in Fig. 6. The MHAP-0.05-600 sample (Fig. 6(a)) exhibits a uniform rice-shaped morphology with a particle size ranging from 50 to 200 nm. The HRTEM image (Fig. 6(b)) clearly reveals the lattice structure of HAP. Moreover, numerous surface pits can be observed on the MHAP-0.05-600 sample, which is consistent with N_2 physical adsorption measurements and previous studies.[47] It should be noted that HAP samples do not possess an interconnected pore structure; hence, the white regions in these TEM images correspond to surface pits on the particles. In Fig. 6(b), distinct lattice fringes are visible for MHAP-0.05-600, with lattice spacings of 0.345 nm matching the crystallographic planes of MoO_3 indexed as {210} and 0.242 nm matching the crystallographic planes of $CaMoO_4$ indexed as {202}, respectively.[48,49] However, no diffraction peak corresponding to MoO_3 appears in the XRD pattern due to its small grain size. When the calcination temperature is increased to 800 °C, the particle size of the catalyst undergoes significant enlargement and the pores on the catalyst surface become indiscernible, indicating that high temperature calcination leads to particle agglomeration. Fig. 6(g) clearly exhibits both the lattice fringe of HAP and $CaMoO_4$, while no lattice fringe of MoO_3 was observed in

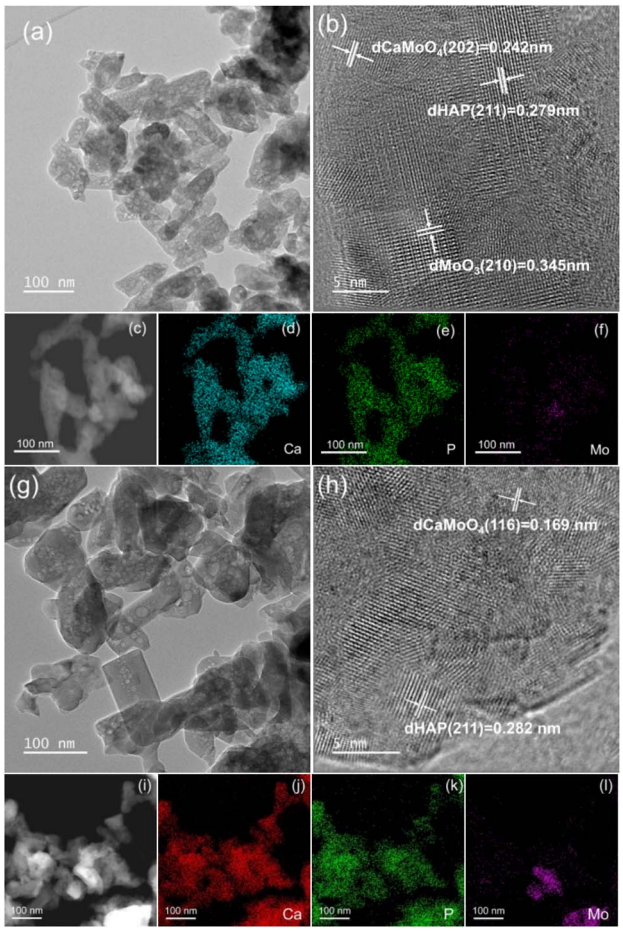

Fig. 6 TEM images and EDS mappings of the MHAP-0.05-600 (a)–(f) and MHAP-0.05-800 (g)–(l) samples.

samples calcinated at 800 °C, further suggesting that high temperature calcination facilitates Mo incorporation into the HAP lattice and nearly eliminates MoO_3. The findings are in accordance with this observation of XRD, XPS, and H_2-TPR. Fig. 6(c–f) and (i–l) present EDS spectra for MHAP-0.05-600 and MHAP-0.05-800 respectively. The results demonstrate even distribution of Mo, Ca, and P in the both samples. Notably, after calcination at high temperatures, molybdenum dispersion in MHAP-0.05-800 is enhanced compared to that in MHAP-0.05-600. These findings indicate an increase in molybdenum dispersion with rising calcination temperature.

Acidities of the MHAP samples

In order to investigate the role of acidity in the ODH reaction, NH_3-TPD spectra of MoO_x/HAP samples were acquired, as depicted in Fig. 7. Two distinct HAP peaks were observed within the temperature range of 130–350 °C and 350–580 °C (Fig. 7(a)), which is consistent with the TPD results of HAP reported in the literature.[50,51] Phosphate groups in HAP are responsible for the acidity of the catalyst, whereas the Ca^{2+} ions are responsible for the basicity. The strong acid site can be ascribed to protons originating from the HPO_4^{2-} group, whereas the weak acid site results from adsorbed water interacting with ammonia through

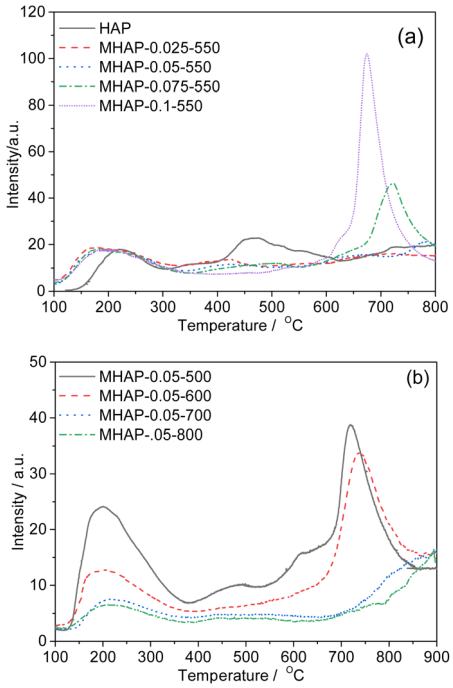

Fig. 7 NH_3-TPD profiles of MHAP samples with different MoO_x loading amounts (a) and calcination temperature (b).

dipole interactions.[52] The low temperature peak of MHAP samples with different MoO_x loading amounts, as shown in Fig. 8(a), exhibits a similar trend to that of HAP, albeit with a slight increase in peak area. In the temperature range of 350–580 °C, the high temperature peak of MHAP samples decreases

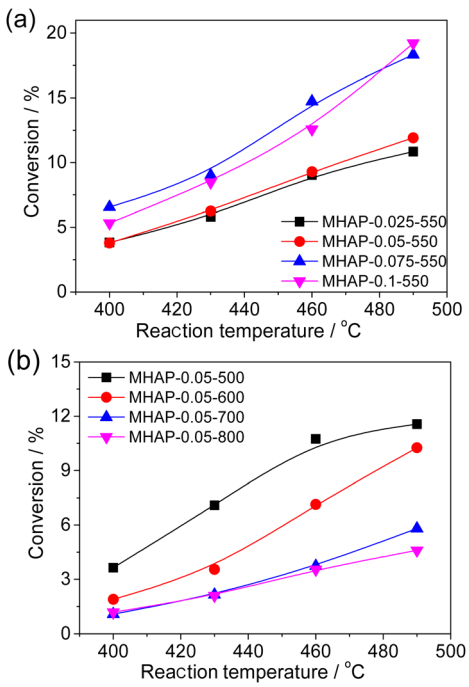

Fig. 8 Catalytic activity of MHAP catalysts with different MoO_x loading amounts (a) and calcination temperature (b).

significantly with an increasing Mo/Ca ratio, and eventually disappears for MHAP-0.1-550 sample due to the coverage of acidic sites on the HAP surface by MoO_x. In addition, a new strong peak was observed in the temperature range of 600–800 °C for samples with high loading amounts (MHAP-0.075-550 and MHAP-0.1-550). This high temperature peak can be attributed to the chemical reaction of MoO_x with NH_3 at high temperatures.

For the samples obtained under different calcination conditions, the intensity of the low temperature peak (130–350 °C) gradually decreases while the high temperature peak (350–580 °C) nearly disappears. This phenomenon can be attributed to the increasing dehydroxylation of HAP with rising calcination temperatures, resulting in a reduction in surface acidity of the sample. Additionally, the enhanced interaction between MoO_x and HAP leads to the formation of P–O–Mo or Ca–O–Mo, resulting in a reduction of the HPO_4^{2-} group. The NH_3 desorption peaks of MHAP-0.05-500 and MHAP-0.05-600 samples are observed within the temperature range of 600–800 °C, while these peaks disappear for MHAP-0.05-700 and MHAP-0.05-800 samples, further confirming the disappearance of MoO_x species under high temperature roasting conditions.

Catalytic performance

The ODH of cyclohexane was investigated over the MoO_x/HAP catalyst in a fixed bed reactor under atmospheric pressure at various temperatures. Fig. 8 illustrates the comparison of activity of MO_x/HAP catalyst. HAP exhibited negligible activity for the ODH of cyclohexane (no shown). The activity of MHAP catalyst initially increased and then slight decreased with increasing Mo loading amounts, indicating that the primary source of ODH activity is derived from MO_x. MHAP-0.75-550 demonstrated the highest activity with a conversion rate of 19.5% at 490 °C. XPS and UV-Vis analysis revealed that isolated, oligomeric MO_x species were predominant at low MoO_x loading amount (MHAP-0.025-550), while there was more polymeric species in addition to oligomeric MoO_x at higher loadings (MHAP-0.05-550, MHAP-0.075-550 and MHAP-0.1-550). This suggests that the activity of isolated, oligomeric MoO_x species is superior to that of MoO_x particles in polymeric state.

The catalyst conversion of MoO_x/HAP decreased significantly with increasing calcination temperature, indicating a strong correlation between the two factors. The conversion of cyclohexane over MHAP-0.05-500 catalyst exhibited an upward trend with the elevation of reaction temperature. Specifically, as the reaction temperature rose from 400 °C to 490 °C, the conversion escalated from 4.8% to 11.8%. When the calcination temperature was increased to 700°, the catalyst activity decreased significantly to only 5.8% at 490 °C. However, when the calcination temperature was further raised to 800 °C, there was minimal change observed in the catalytic activity. These observed catalytic properties can be attributed to the specific type and structure of the active components present in the catalyst. The form of Mo in the sample changed from Mo^{5+} to Mo^{6+} as the calcination temperature increased from 500 °C to 600 °C, indicating that Mo^{5+} exhibited higher ODH activity compared to Mo^{6+}. Furthermore, with an increase in calcination temperature up to 700 °C, there was a gradual strengthening of interaction between MoO_x and the carrier. The interaction between MoO_x and the carrier gradually intensified as the calcination temperature increased to 700 °C, leading to a higher substitution of P in HAP by Mo and resulting in the formation of well-dispersed P–O–Mo or Ca–O–Mo species. However, it should be noted that both MHAP-0.05-700 and MHAP-0.05-800 samples displayed low conversion rates due to lower ODH activity associated with P–O–Mo or Ca–O–Mo. In addition, the NH_3-TPD results revealed a significant reduction in the surface acidity of MHAP-0.05-800. Since the cleavage of C–C bonds during ODH of cyclohexane is closely associated with acidity, the observed decrease in conversion rate can be attributed to the decline in acidity.

Fig. 9(a) and (b) depict the product selectivity of the cyclohexane ODH reaction at a temperature of 460 °C. There are three potential reactions in the ODH of cyclohexane:[4] (1) partial ODH of cyclohexane yields cyclohexene, which can subsequently undergo further dehydrogenated to benzene; (2) direct dehydrogenation of cyclohexane to benzene, followed by peroxidation to CO_x; (3) direct peroxidation of cyclohexane to CO_x. Cyclohexene can be considered as an intermediate product in the ODH process of cyclohexane, thus the selectivity towards cyclohexene is influenced by both the catalyst's dehydrogenation ability and the desorption capability of cyclohexene. The results depicted in Fig. 9(a) demonstrate that MHAP with a low MoO_3 loading amount exhibits high selectivity towards cyclohexene and CO_x. This suggests that the reaction rates of route (1) and route (3) are elevated in the MHAP-catalyzed ODH reaction system, indicating that the MHAP catalyst possesses an appropriate ODH capacity. However, the high CO_x selectivity of MHAP with a low MoO_3 loading amount also indicates its strong

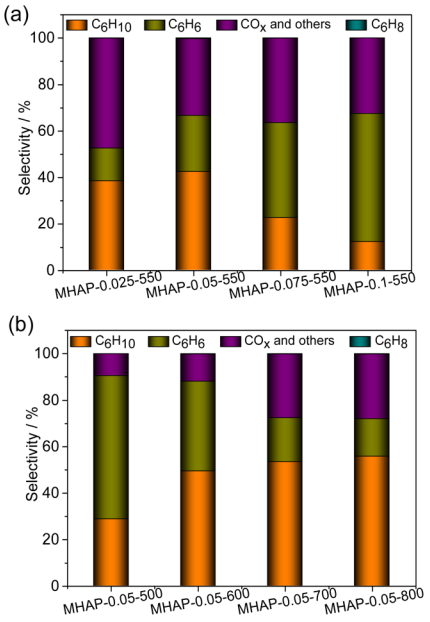

Fig. 9 The product distribution patterns of the MHAP catalysts with different MoO_x loading amounts (a) and calcination temperature (b).

capability in breaking C–H bonds, which is closely associated with the strong acidity of MHAP. The MoO_x/HAP samples with low loading amount exhibited a pronounced preference for cyclohexene production, suggesting that the high dispersion of MoO_x and Mo^{5+} species played a crucial role in enhancing selectivity. The MoO_x/HAP samples exhibited high selectivity towards benzene, with an increase in benzene selectivity observed as the amount of MoO_x impregnation increased. This suggests that MoO_x/HAP possesses a strong oxidative dehydrogenation capacity.

The selectivity of cyclohexene exhibited significant variations among MoO_x/HAP samples calcined at different temperatures, with the low-temperature calcination samples (MHAP-0.05-500 and MHAP-0.05-600) differing notably from the high-temperature calcination samples (MHAP-0.05-700 and MHAP-0.05-800). This discrepancy can be attributed to the distinct chemical environments surrounding the molybdenum species. The selectivity of cyclohexene increased proportionally with the rise in calcination temperature, ultimately reaching 58.2% in the MHAP-0.05-800 sample. The selectivity of cyclohexene is significantly higher compared to the previously reported cyclohexane ODH reaction.[10,53–55] The impact of Mo^{5+} and Mo^{6+} on the activity and selectivity of oxidative dehydrogenation of cyclohexane has been demonstrated in various studies. The internal structure of MoO_3 contains a significant number of oxygen vacancies, and it maintains a dynamic equilibrium between the structural defects and gas phase oxygen through REDOX reactions involving Mo^{5+} and Mo^{6+}.[56,57] The octahedral structure of Mo^{6+} promotes deep oxidation reactions, and catalysts with higher Mo^{5+} content exhibit excellent catalytic activity in oxidative dehydrogenation reactions. Moreover, the unsaturated coordination structure of Mo^{5+} contributes to enhanced olefin selectivity. Although the proportion of Mo^{6+} in highly calcined samples increased, the elevated calcination temperature facilitated the incorporation of Mo into HAP lattice, resulting in the formation of P–O–Mo or Ca–O–Mo species. This observation implies that highly dispersed P–O–Mo or Ca–O–Mo species are more favorable for olefin production. The successive increase in calcination temperature leads to a decrease in acidic sites, thereby facilitating the desorption of cyclohexene and inhibiting its further oxidation to benzene and CO_x. The MHAP-0.05-700 and MHAP-0.05-800 catalysts exhibited high selectivity towards cyclohexene and CO_x, indicating that pathways (1) and (3) had higher reaction rates in the MHAP-catalyzed ODH reaction system. This suggests that the MHAP catalyst possesses suitable ODH capacity. However, the elevated CO_x selectivity also implies that MHAP exhibits a strong ability to break C–H bonds, which is attributed to its pronounced acidity.

The relationship between selectivity and conversion of C_6H_{10}, C_6H_6, and CO_x at different reaction temperatures on MoO_x/HAP is illustrated in Fig. 10. The selectivity of various catalysts for C_6H_6 and CO_x decreases as the conversion rate increases, while the selectivity of different catalysts for cyclohexene exhibits a distinct correlation with the conversion rate. The selectivity of C_6H_{10} increases with the increase in conversion rate for MHAP-0.05-500 catalysts, indicating that benzene

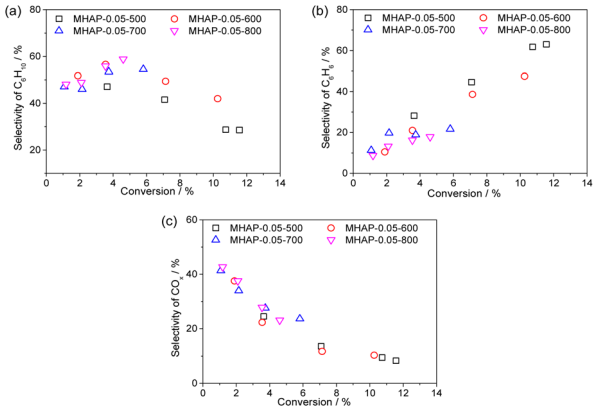

Fig. 10 The selectivity–conversion relationships for cyclohexane ODH over different catalysts. (a) C_6H_{10}, (b) C_6H_6 and (c) CO_x.

is primarily formed through cyclohexene intermediates. The selectivity of C_6H_6 increases with the rise in conversion, attributed to the elevated reaction temperature. The enhanced lattice oxygen mobility at elevated temperatures suggests that the nucleophilic lattice oxygen in the catalyst becomes more advantageous for the dehydrogenation process, thereby promoting the conversion of intermediate cyclohexene into thermodynamically stable benzene. The selectivity of C_6H_{10} on the MHAP-0.05-600 catalyst exhibits irregular variations with increasing conversion. The catalytic properties of MHAP-0.05-700 and MHAP-0.05-800 samples demonstrate the influence of P–O–Mo and Ca–O–Mo on product selectivity. In the case of MHAP-0.05-800 samples, the selectivity towards C_6H_6 and C_6H_{10} increases with increasing conversion, while the selectivity towards CO_x decreases, suggesting that C_6H_6 is formed through direct dehydrogenation of cyclohexane, whereas CO_x may be generated through oxidation of cyclohexane and benzene.

Conclusions

Two series of MoO_x/HAP catalysts with different MoO_x loading amounts and calcination temperature were prepared by impregnation method. The MoO_x/HAP catalyst was characterized using XRD, XPS, UV-Vis, and H_2-TPR. MoO_x/HAP catalysts with lower loading exhibited higher dispersion and a greater proportion of Mo^{5+} species, whereas those with higher loading showed an increased presence of Mo^{6+} species. The MoO_x/HAP obtained at a low calcination temperature primarily consists of surface MoO_x and contains a higher proportion of Mo^{5+} species. However, upon high calcination, the Mo^{5+} species undergo transformation to Mo^{6+}, and the interaction between MoO_x and HAP carrier leads to the substitution of P positions in the HAP lattice by Mo, resulting in the formation of P–O–Mo or Ca–O–Mo structures. The MoO_x/HAP catalysts were employed for the catalysis of cyclohexane ODH to cyclohexene. The MoO_x/HAP catalysts with lower loading amount exhibited reduced cyclohexane conversion and enhanced selectivity towards cyclohexene, suggesting that the presence of Mo^{5+} species promotes olefin production. The conversion of catalysts calcined at low

temperature was found to be higher than that of catalysts calcined at high temperature, whereas the selectivity towards cyclohexene was observed to be higher for MHAP-0.05-700 and MHAP-0.05-800 catalysts. At a reaction temperature of 430 °C, when the conversion rate of cyclohexane reached 13.1%, the selectivity of MHAP-0.05-800 towards cyclohexene achieved 58.2%. The high selectivity is directly influenced by the chemical environment of MoO_x species, where dispersed P–O–Mo or Ca–O–Mo species are more favorable for olefin production. Moreover, the high-temperature calcination-induced decrease in acidity results in a reduction of the adsorption capacity of MoO_x/HAP for cyclohexene, thereby promoting its desorption on the catalyst surface, inhibiting deep oxidation and enhancing selectivity.

Data availability

All data and related metadata underlying the findings reported in a submitted manuscript should be deposited in an appropriate public repository, unless already provided as part of the submitted article.

Conflicts of interest

The authors declare no conflict of interests.

Acknowledgements

This work was supported by the National Natural Science Foundation of China (No. 201905081).

References

1 H. Yu, F. Peng, J. Tan, X. Hu, H. Wang, J. Yang and W. Zheng, *Angew. Chem., Int. Ed.*, 2011, **50**, 3978–3982.
2 A. P. Unnarkat, T. Sridhar, H. Wang, S. Mahajani and A. K. Suresh, *AlChE J.*, 2016, **62**, 4384–4402.
3 C. Resini, M. Panizza, F. Raccoli, M. Fadda, M. M. Carnasciali, G. Busca, E. F. Lopez and V. S. Escribano, *Appl. Catal., A*, 2003, **251**, 29–38.
4 H. Feng, J. W. Elam, J. A. Libera, M. J. Pellin and P. C. Stair, *J. Catal.*, 2010, **269**, 421–431.
5 Y. Gambo, S. Adamu, A. A. Abdulrasheed, R. A. Lucky, M. S. Ba-Shammakh and M. M. Hossain, *Appl. Catal., A*, 2021, **609**, 117914.
6 Z. Fu, D. Z. Li, L. D. Zhou, Y.-M. Li, J. W. Guo, Y. Q. Li, H.-M. Liu and Q. J. Zhang, *Pet. Sci.*, 2023, **20**, 2488–2498.
7 X. Song, F. Zhou, H. Ma, Y. Liu and G. Wu, *Mol. Catal.*, 2023, **542**, 113105.
8 S. Kumar, A. Qadir, F. Maury and N. Bahlawane, *ACS Appl. Mater. Interfaces*, 2017, **9**, 21447–21456.
9 D. Contreras, V. Melin, K. Márquez, G. Pérez-González, H. D. Mansilla, G. Pecchi and A. Henríquez, *Appl. Catal., B*, 2019, **251**, 17–24.
10 I. A. Samek, N. S. Bobbitt, R. Q. Snurr and P. C. Stair, *J. Catal.*, 2020, **384**, 147–158.
11 V. Vaiano, D. Sannino, A. R. Almeida, G. Mul and P. Ciambelli, *Catalysts*, 2013, **3**, 978–997.
12 S. A. Kadam, S. Sandoval, Z. Bastl, K. Simkovičová, L. Kvítek, J. Jašík, J. E. Olszówka, S. Valtera, M. Vaidulych, J. Morávková, P. Sazama, D. Kubička, A. Travert, J. A. van Bokhoven, A. Fortunelli, A. Kleibert, M. Kalbáč and Š. Vajda, *ACS Catal.*, 2023, **13**, 13484–13505.
13 S. Lee, A. Halder, G. A. Ferguson, S. Seifert, R. E. Winans, D. Teschner, R. Schlögl, V. Papaefthimiou, J. Greeley, L. A. Curtiss and S. Vajda, *Nat. Commun.*, 2019, **10**, 954.
14 B. Sarkar, C. Pendem, L. N. S. Konathala, T. Sasaki and R. Bal, *Catal. Commun.*, 2014, **56**, 5–10.
15 X. Chen, X. Su, H. Duan, B. Liang, Y. Huang and T. Zhang, *Catal. Today*, 2017, **281**, 312–318.
16 G. J. Hutchings, A. Desmartin-Chomel, R. Olier and J.-C. Volta, *Nature*, 1994, **368**, 41–45.
17 A. Ebadi, N. Safari and M. H. Peyrovi, *Appl. Catal., A*, 2007, **321**, 135–139.
18 S. Goergen, C. Yin, M. Yang, B. Lee, S. Lee, C. Wang, P. Wu, M. B. Boucher, G. Kwon, S. Seifert, R. E. Winans, S. Vajda and M. Flytzani-Stephanopoulos, *ACS Catal.*, 2013, **3**, 529–539.
19 G. W. Coulston, S. R. Bare, H. Kung, K. Birkeland, G. K. Bethke, R. Harlow, N. Herron and P. L. Lee, *Science*, 1997, **275**, 191–193.
20 L. E. Cadus, M. F. Gomez and M. C. Abello, *Catal. Lett.*, 1997, **43**, 229–233.
21 E. Heracleous, A. F. Lee, I. A. Vasalos and A. A. Lemonidou, *Catal. Lett.*, 2003, **88**, 47–53.
22 M. C. Abello, M. F. Gomez and O. Ferretti, *Appl. Catal., A*, 2001, **207**, 421–431.
23 K. Chen, A. T. Bell and E. Iglesia, *J. Phys. Chem. B*, 2000, **104**, 1292–1299.
24 E. Heracleous, J. Vakros, A. A. Lemonidou and C. Kordulis, *Catal. Today*, 2004, **91–92**, 289–292.
25 F. R. Brown, L. E. Makovsky and K. H. Rhee, *J. Catal.*, 1977, **50**, 162–171.
26 L. Wang and W. K. Hall, *J. Catal.*, 1983, **83**, 242–244.
27 Y. C. Xie and Y. Q. Tang, Spontaneous Monolayer Dispersion of Oxides and Salts onto Surfaces of Supports: Applications to Heterogeneous Catalysis, *Adv. Catal.*, 1990, **37**, 1–43.
28 J. A. Bergwerff, T. Visser, G. Leliveld, B. D. Rossenaar, K. P. de Jong and B. M. Weckhuysen, *J. Am. Chem. Soc.*, 2004, **126**, 14548–14556.
29 O. P. Oni, Y. Hu, S. Tang, H. Yan, H. Zeng, H. Wang, L. Ma, C. Yang and J. Ran, *Mater. Chem. Front.*, 2023, **7**, 9–43.
30 C. Boucetta, M. Kacimi, A. Ensuque, J. Y. Piquemal, F. Bozon-Verduraz and M. Ziyad, *Appl. Catal., A*, 2009, **356**, 201–210.
31 C. Li, G. Xu, X. Liu, Y. Zhang and Y. Fu, *Ind. Eng. Chem. Res.*, 2017, **56**, 8843–8849.
32 G. Xu, Y. Zhang, Y. Fu and Q. Guo, *ACS Catal.*, 2017, **7**, 1158–1169.
33 S. Sugiyama, T. Osaka, Y. Hirata and K. I. Sotowa, *Appl. Catal., A*, 2006, **312**, 52–58.
34 K. E. Kabouss, M. Kacimi, M. Ziyad, S. Ammar, A. Ensuque, J. Y. Piquemal and F. Bozon-Verduraz, *J. Mater. Chem.*, 2006, **16**, 2453–2463.

35 S. Huang, T. Ouyang, B.-F. Zheng, M. Dan and Z.-Q. Liu, *Angew. Chem., Int. Ed.*, 2021, **60**, 9546–9552.
36 J. Dou and H. C. Zeng, *J. Am. Chem. Soc.*, 2012, **134**, 16235–16246.
37 I. A. de Castro, R. S. Datta, J. Z. Ou, A. Castellanos-Gomez, S. Sriram, T. Daeneke and K. Kalantar-zadeh, *Adv. Mater.*, 2017, **29**, 1701619.
38 W. Du, Y. Shi, W. Zhou, Y. Yu and B. Zhang, *Angew. Chem., Int. Ed.*, 2021, **60**, 7051–7055.
39 K. Cui, L. Yang, Z. Ma, F. Yan, K. Wu, Y. Sang, H. Chen and Y. Li, *Appl. Catal., B*, 2017, **219**, 592–602.
40 S. Chen, C. Pei, X. Chang, Z.-J. Zhao, R. Mu, Y. Xu and J. Gong, *Angew. Chem., Int. Ed.*, 2020, **59**, 22072–22079.
41 D. Wang, L. Jin, Y. Li and H. Hu, *Fuel*, 2017, **210**, 803–810.
42 J. Cao, T. Nakamura, T. Kitazawa, N. Yamashiki, T. Yamamoto and T. Taneike, *Prostaglandins Other Lipid Mediators*, 2008, **86**(1–4), 26–34.
43 A. Chakrabarti and I. E. Wachs, *ACS Catal.*, 2018, **8**, 949–959.
44 L. O. Alemán-Vázquez, F. Hernández-Pérez, J. L. Cano-Domínguez, A. Rodríguez-Hernández and J. L. García-Gutiérrez, *Fuel*, 2014, **117**, 463–469.
45 M. Saghafi, S. Heshmati-Manesh, A. Ataie and A. A. Khodadadi, *Int. J. Refract. Met. Hard Mater.*, 2012, **30**, 128–132.
46 E. Cheng and J. Notestein, *J. Catal.*, 2021, **397**, 212–222.
47 Y. Sun, Z. Qu, D. Chen, H. Wang, F. Zhang and Q. Fu, *Chin. J. Catal.*, 2014, **35**, 1927–1936.
48 S. Zhang, G. Wang, J. Jin, L. Zhang, Z. Wen and J. Yang, *Nano Energy*, 2017, **36**, 186–196.
49 Y. Wu, W. Liu, Z. Zhang, Y. Zheng, X. Fu, J. Lu, S. Cheng, J. Su and Y. Gao, *Energy Storage Mater.*, 2023, **61**, 102849.
50 B. Yan, L. Z. Tao, Y. Liang and B. Q. Xu, *ACS Catal.*, 2014, **4**, 1931–1943.
51 V. C. Ghantani, S. T. Lomate, M. K. Dongare and S. B. Umbarkar, *Green Chem.*, 2013, **15**, 1211–1217.
52 N. S. Resende, M. Nele and V. M. M. Salim, *Thermochim. Acta*, 2006, **451**, 16–21.
53 P. Du, X. X. Zhang, S. Zhang, Y. Zhao, L. Zhang, B. Zhang and B. Yang, *ChemCatChem*, 2021, **13**, 610–616.
54 J. Wang, C. Wan, D. G. Cheng, F. Chen and X. Zhan, *Appl. Surf. Sci.*, 2021, **565**, 150609.
55 N. L. Wang, J. E. Qiu, Z. W. Wu, J. Wu, K. Y. You and H. A. Luo, *Appl. Catal., A*, 2015, **503**, 62–68.
56 K. Murugappan, E. M. Anderson, D. Teschner, T. E. Jones, K. Skorupska and Y. Román-Leshkov, *Nat. Catal.*, 2018, **1**, 960–967.
57 T. Hu, B. Xue, F. Meng, L. Ma, Y. Du, S. Yu, R. Ye, H. Li, Q. Zhang, L. Gu, Z. Zhou, R. Liang and C. Tan, *Adv. Healthcare Mater.*, 2023, **12**, 2202911.